# Growth, Structure, and Stability of Au on Ordered ZrO$_2$(111) Thin Films

Yonghe Pan, Yan Gao, Guodong Wang, Dandan Kong, Liang Zhang, Jianbo Hou, Shanwei Hu, Haibin Pan, and Junfa Zhu*

National Synchrotron Radiation Laboratory, University of Science and Technology of China, Hefei, Anhui 230029, China

ABSTRACT: The growth, electronic properties, and thermal stability of Au nanoparticles on ordered ZrO$_2$(111) thin film surfaces were investigated by low-energy electron diffraction (LEED), X-ray photoelectron spectroscopy (XPS), and synchrotron radiation photoemission spectroscopy (SRPES). The thin ZrO$_2$(111) films were grown on a Pt(111) substrate. At room temperature, Au initially grows as 2D islands on the ZrO$_2$(111) thin films up to 0.1 ML, followed by 3D growth with a number density of ~1.4 × 10^{12} particles/cm^2. The binding energy of the Au 4f peaks shifts monotonically toward a higher binding energy with decreasing the Au particle size by 0.4 eV, which can be attributed to the contribution from both the initial- and final-state effects. Au atoms most likely form Au$^{\delta-}$ initially and become metallic states as the coverage increases. Thermal annealing experiments demonstrate that Au particles experience significant sintering before desorption from the ZrO$_2$(111) surface. In addition, Au particles are more thermally stable on the sputtered ZrO$_2$(111) surface than on the pristine ZrO$_2$(111) surface due to the stronger bonding of Au atoms on the surface defect sites. Moreover, large Au particles are more thermally stable than small ones on the ZrO$_2$(111) surface.
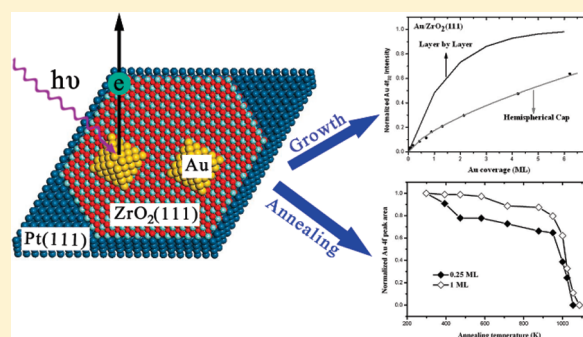
1. INTRODUCTION

Since Haruta et al.[1,2] first reported that gold nanoparticles supported on metal oxides exhibited high activity toward low-temperature CO oxidation, the studies of oxide-supported gold catalysts have received significant attention.[3] Despite great progress made in the studies of gold-catalyzed reactions, the origins of the catalytic activities, interfacial structures, and the nature of Au chemical states related to the oxide-supported Au catalysts are still subjects of debate. For example, it has been recognized for a long time that Au nanoparticles supported on reducible oxides (e.g., TiO$_2$, CeO$_2$) exhibit much higher activity than those on irreducible oxides (e.g., MgO, Al$_2$O$_3$, SiO$_2$) for CO oxidation.[4−6] It was therefore thought that the oxide supports play a vital role in the catalytic reactions. However, this correlation between the activity of supported Au catalysts and the type of oxide supports (reducible/irreducible) has been questioned by recent experiments. Liotta and co-workers observed that the catalyst of Au supported on irreducible oxide Al$_2$O$_3$ shows higher CO oxidation activity in the presence of hydrogen at low temperature as compared to that of Au on reducible oxide TiO$_2$.[7] Moreover, Ivanova et al. reported that Au supported on Al$_2$O$_3$ has higher activity in preferential oxidation of CO than it does supported on reducible oxide CeO$_2$.[8] Obviously, the differences in the above-mentioned catalysts' activities cannot be solely attributed to the effects of the oxide supports and are still not well understood. Furthermore, among the Au catalysts, the oxidation states of Au species are still under discussion. Some authors ascribed the active Au component of Au/ceria catalysts in the water gas shift (WGS) reactions to the cationic Au sites,[9,10] whereas others attributed the active phase of gold to small metallic particles.[11,12]

Therefore, the clarification of the chemical states of oxide-supported Au species and the studies of the Au−oxide support interaction are of great importance.

Zirconium oxide is of significant interest in catalytic applications, especially as catalyst supports for various reactions because of its ideal chemical and mechanical properties.[13−15] The most important catalytic application of ZrO$_2$ is used as an additive in the three-way catalyst (TWC), where it serves to improve ceria stability and its oxygen storage capacity (OSC).[16,17] Highly dispersed gold supported on zirconia has been reported to show exceptional catalytic properties for a number of reactions such as CO oxidation,[18,19] WGS reactions,[13,20] and selective hydrogenation of unsaturated organic compounds.[21,22] The perimeter interface between Au and ZrO$_2$ plays an essential role in determining the catalytic reactivity.[23] Zhang et al. found that increasing Au−ZrO$_2$ contact boundaries by reducing the sizes of zirconia nanoparticles can enhance the catalytic activity for CO oxidation.[24] This finding is in good agreement with the result of Idakiev and co-workers, where they attributed the high WGS activity to the contact boundaries between Au and zirconia.[13] In addition, it has also been found that the chemical state of gold,[15] the sizes of both gold and zirconia,[24,25] and the zirconia crystal phase[14] have great impacts on the catalytic activity. Therefore, it is very important to study the structure and properties of the Au−ZrO$_2$ interface. However, few studies of the Au−ZrO$_2$ interface can be found. Zafeiratos et al. studied experimentally

Au deposition on yttria-stabilized $ZrO_2(100)$ (YSZ) and found that the interaction between Au and ZrO_2 is very weak,[26] which is also confirmed by Munoz et al.,[27] where the strength of the bond at the Au–YSZ interface calculated by the contact angle is very weak. The adsorption of Au atoms at well-defined $ZrO_2(111)$ surfaces and the small Au clusters at various zirconia surfaces have been investigated theoretically by Grau-Crespo et al.[28] and Wang et al.,[29] respectively. To our knowledge, no experimental work on the growth of Au on pure ordered $ZrO_2(111)$ surfaces under ultrahigh vacuum (UHV) conditions can be found so far.

In our previous work, well-ordered $ZrO_2(111)$ films epitaxially grown on Pt(111) were successfully obtained.[30] Such films have been proven to present a cubic phase,[31,32] which can be stabilized only at 2650–2950 K for pure zirconia or at low temperature by doping with lower-valence cations (e.g., Ca^{2+}, Mg^{2+}, and Y^{3+}).[33] Herein, we extend the application of the stable cubic $ZrO_2(111)$ films as model surfaces for surface science studies of Au interaction with ZrO_2 at room temperature. Synchrotron radiation photoemission spectroscopy (SRPES), X-ray photoelectron spectroscopy (XPS), and low energy electron diffraction (LEED) have been employed to investigate the growth, structure, and interfacial electronic properties of Au on $ZrO_2(111)$, with the aim of gaining a deep insight into the relationship between the structure and the chemical properties of zirconia-supported gold catalysts at an atomic level.

2. EXPERIMENTAL SECTION

All of the experiments were performed on a UHV system located at the photoemission endstation at beamline U20 in the National Synchrotron Radiation Laboratory (NSRL) in Hefei, China. The beamline is connected to a bending magnet and equipped with three gratings that cover photon energies from 60 to 1000 eV with a resolving power ($E/\Delta E$) better than 1000. The UHV system consists of three separate chambers for sample analysis, preparation, and quick load-lock. The analysis chamber, with a base pressure less than 2×10^{-10} Torr, is equipped with a VG SCIENTA R3000 electron energy analyzer, a twin anode (Mg and Al) X-ray source, a retractable four-grid optics for low energy electron diffraction (LEED), and an Ar^+ sputter gun. The preparation chamber has a base pressure of ~3×10^{-10} Torr and houses with a four-pocket electron beam evaporator for Zr, where a stable and long-term evaporation can be easily achieved via a flux controller, and a home-built evaporator for Au. The sample quick load-lock port is connected to the preparation chamber.

The sample was clamped to a molybdenum holder by two spot-welded Ta strips and heated from the backside of the sample using electron-beam bombardment. The sample temperature was monitored using a K type thermocouple that was fixed on the edge of the sample holder plate. The reading of this thermocouple was calibrated separately by another thermocouple that was spot-welded directly to the edge of the sample. The Pt(111) single crystal (10 mm diameter and 1 mm thick, purchased from Mateck GmbH, Germany) was cleaned by repeated cycles of Ar^+ ion sputtering, annealing in 1×10^{-7} Torr of oxygen at 800 K to remove carbon, and then flashing to 1300 K to remove oxygen, until no contamination was detected by XPS and a sharp (1 × 1) LEED pattern was achieved.[34]

The thin $ZrO_2(111)$ film was grown by evaporating Zr metal from a Mo crucible using the electron beam evaporator onto the clean Pt(111) surfaces in oxygen atmosphere at 550 K, followed
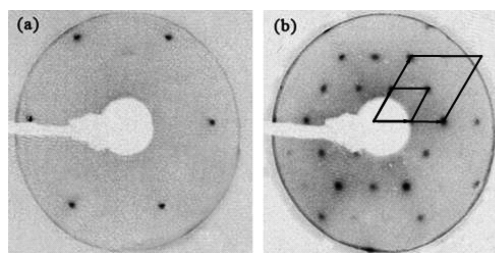

Figure 1. LEED patterns at 64 eV for (a) clean Pt(111) and (b) 3.4 nm thick ZrO_2 film on Pt(111). The characteristics of the hexagonal p(1 × 1) and p(2 × 2) structures of $ZrO_2(111)$ are indicated in (b).

by annealing. Details of the preparation and characterization of the $ZrO_2(111)$ films have been described previously.[30] The evaporation rate was limited to 0.06 nm per minute. From the attenuation of Pt 4f signals, the thickness of the $ZrO_2(111)$ film was estimated. In the present study, the $ZrO_2(111)$ film was controlled to be about 3–4 nm thick to avoid the surface charging.[30]

The deposition of Au onto $ZrO_2(111)$ was performed at a sample temperature of 300 K by evaporating high-purity Au (better than 99.999%) from a homemade electron beam evaporator in the preparation chamber. A very slow evaporation rate (0.12 ± 0.01 Å/min) of Au was used in our experiments. The evaporation rate was kept constant in all cases and was estimated from the attenuation of the Pt 4f peak intensities after Au was directly deposited on Pt(111). The Au coverage was presented in this article as equivalent monolayers (ML), which are defined as the density of close-packed Au(111) layer, that is, 1 ML = 1.4×10^{15} atoms/cm². The monolayer thickness is approximately 2.6 Å.[33] After each deposition, the sample was quickly transferred to the analysis chamber for the photoelectron spectroscopy (PES) measurements.

The photoemission spectra were collected at 10° emission from the surface normal. Au 4f spectra were measured with a photon energy of 150 eV. Al Kα (1486.6 eV) was used to probe Zr 3d and O 1s core levels. Valence spectra were recorded with a photon energy of 70 eV. All of the binding energies (BE) were referenced to the Au $4f_{7/2}$ peak position at 84 eV from a clean polycrystalline Au foil, which was mounted below the sample position on the sample holder.

3. RESULTS AND DISCUSSION

3.1. Thin $ZrO_2(111)$ Films. The detailed preparation procedure of ZrO_2 films on Pt(111) has been reported previously.[30] The quality of the films was verified by XPS and LEED. Quantitative analysis of XPS suggested that stoichiometric ZrO_2 was obtained. On the basis of previous reports,[30,31,35] continuous $ZrO_2(111)$ films of high quality are formed when the film thickness is above 2 nm. Part a of Figure 1 displays a sharp LEED pattern of the clean Pt(111) surface. After deposition of a 3.4 nm thick ZrO_2 film, a nonrotated hexagonal p(1 × 1) of $ZrO_2(111)$ structure that coexists with a (2 × 2) pattern is observed yet without the diffraction pattern of the Pt(111) substrate (part b of Figure 1), indicating that the ZrO_2 film of high structural order are continuous and cover the whole Pt(111) surface. This film provides a good model surface for bulk ZrO_2, which is used as the substrate for Au deposition in this study.
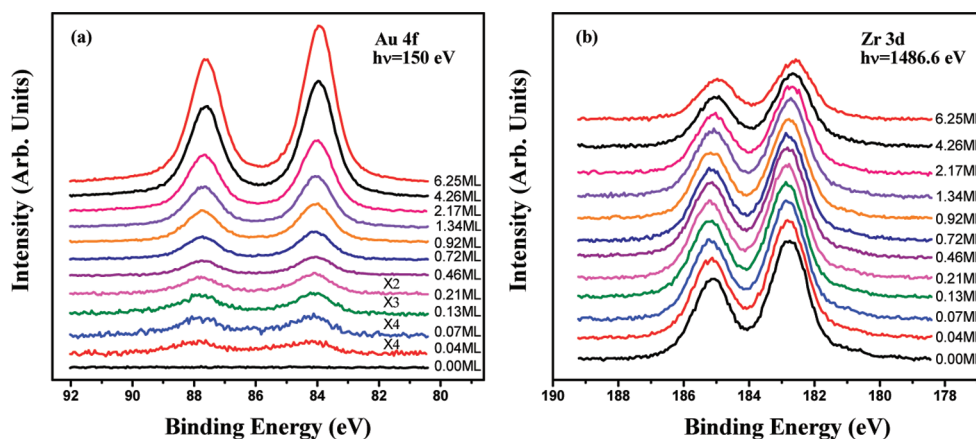
Figure 2. Au 4f (a) and Zr 3d (b) spectra for Au growth on $ZrO_2(111)$ at room temperature at different Au coverages. The photon energies for Au 4f and Zr 3d are 150 and 1486.6 eV, respectively.
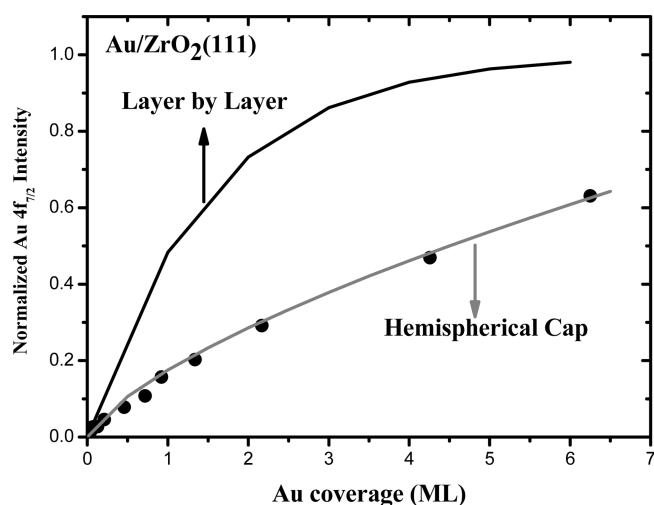

Figure 3. Integrated Au $4f_{7/2}$ (●) intensity normalized to that of bulk Au versus Au coverage for the room temperature growth of Au on a 3.4 nm thick $ZrO_2(111)$ film grown on Pt(111). The solid curves correspond to what is expected if the Au film growth in a layer-by-layer growth model or a hemispherical cap growth model with an island density of 1.4×10^{12} islands/cm^2, respectively. The inelastic mean free path used for calculating the two solid curves is 0.4 nm, taken from the fitted curve in ref 38.

3.2. Growth Mode of Au on Thin $ZrO_2(111)$ Films. Figure 2 shows Au 4f and Zr 3d core-level photoemission spectra as a function of Au coverage on the $ZrO_2(111)$ thin film surface at room temperature. As expected, the Au 4f peak intensities grow with increasing Au coverage, whereas the intensity of the Zr 3d peak decreases. When the Au coverage increases to 6.25 ML, the intensity of Zr 3d decreases by a factor of 0.54 ± 0.05. Simultaneously, almost the same attenuation of O 1s intensities is observed in the O 1s XPS spectra (not shown). If Au grows two dimensionally on $ZrO_2(111)$, both Zr 3d and O 1s signals should only remain 34.6% of the original intensities after 6.25 ML Au deposition. The fact of that the intensity of the substrate signal is kept by ~46% after deposition of 6.25 ML Au may suggest that Au grows three dimensionally on $ZrO_2(111)$.

To further address the growth mode of Au on $ZrO_2(111)$, the Au 4f intensities during the successive Au deposition on

$ZrO_2(111)$ at room temperature are plotted as a function of Au coverage, as shown in Figure 3. The closed circles represent the experimental data of Au $4f_{7/2}$ intensities that have been normalized to a bulklike Au signal on $ZrO_2(111)$. It is clear that the intensity of the Au peak increases continuously with the Au coverage without any distinct breaks. Using a layer-by-layer growth model[36] and a 3D-particle (hemispherical cap) growth model with an assumption of constant island density,[37] we have calculated the expected results. The intensity ratios in these two models are given as follows, respectively:

$$\frac{I_{Au}}{I_{Au}(\infty)} = 1 - \exp(-d/\lambda_{Au} \cos \theta) \quad (1)$$

$$\frac{I_{Au}}{I_{Au}(\infty)} = nR^2\pi$$
$$- 2\pi n\lambda_{Au}^2 \cos^2\theta\left[1 - \left(1 + \frac{R}{\lambda_{Au} \cos \theta}\right) \exp\left(-R/\lambda_{Au}\cos\theta\right)\right]$$
$$(2)$$

where I_{Au} represents the Au $4f_{7/2}$ intensity and $I_{Au}(\infty)$ is the Au intensity from a thick bulklike Au layer on $ZrO_2(111)$, d is the Au thickness, λ_{Au} is the mean free path of Au photoelectrons, θ is the detection angle with respect to the surface normal ($\theta = 10°$ in this work), and R and n are the radius and the number density of the hemispherical Au particles, respectively. Here, in the hemispherical cap model, the number density is assumed to be independent of coverage and treated as a constant for fitting. Thus, the average diameter and volume of Au particles are set by this density at any given Au coverage. For example, at 0.4 ML the average Au particle size is calculated to be 3.0 nm in diameter. The inelastic mean free path used is 0.4 nm, obtained from a fitted curve according to the data reported by Tanuma et al.[38]

As can be seen in Figure 3, in the early stages of Au deposition (<0.1 ML) on $ZrO_2(111)$ at room temperature, the Au signals change along a slope close to that expected for layer-by-layer growth, suggesting that Au initially may grow two dimensionally on $ZrO_2(111)$. As the coverage increases to 0.1 ML and above, the increase of Au signal clearly deviates from that expected for the layer-by-layer model. Instead, the signal fits very well with the hemispherical cap model with an assumed constant number density of 1.4×10^{12} islands/cm^2, again demonstrating that Au grows as 3D islands on the $ZrO_2(111)$ substrate. A similar
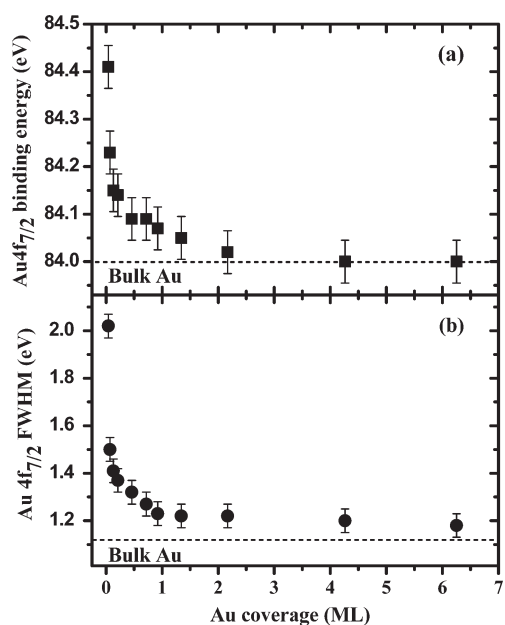
Figure 4. (a) Variation in the Au $4f_{7/2}$ binding energy as a function of Au coverage, (b) variation in the Au $4f_{7/2}$ fwhm as a function of Au coverage.

growth mode has also been observed for Au deposition on TiO_2[39,40] and YSZ(100)[26] at 300 K.

It is known that the growth mode of a metal on an oxide surface can be also thermodynamically predicted from the surface free energies of deposited metal (γ_m), the oxide (γ_{ox}), and the metal−oxide interface (γ_{m-ox}).[41] If $\gamma_{ox} < \gamma_m + \gamma_{m-ox}$, the growth of metal on oxide follows Volmer−Weber (VW) or 3D growth mode. Otherwise, a continuous metal film is formed; the metal growth follows layer-by-layer (Frank van der Merwe, FM) or layer-followed-by-clusters (Stranski−Krastanov, SK) mode. The surface free energy of Au is 1.13 J/m^2,[42] which is much larger than that of ZrO_2 ($\sim$0.7 J/m^2).[43] Thus, in the absence of kinetic limitations, a continuous Au film formation on ZrO_2(111) is not thermodynamically possible, unless the interfacial free energy γ_{m-ox} between Au and ZrO_2(111) is a large negative value. Usually, the real interfacial energies at the metal−oxide interfaces are positive, even good bonding between phases at the interface of metal−oxide would lead γ_{m-ox} to be small positive values.[41] Therefore, a 3D growth of Au on ZrO_2(111) is thermodynamically favored. This is in accordance with our experimental result. At very low coverages (<0.1 ML), however, Au grows as 2D islands, probably due to the fact that Au initially populates the defect sites such as step edges and kinks.[44] This is very common for metal growth on oxide films.[41] This 2D growth observed at very low coverages can be interpreted as a consequence of surface kinetic constraints.[39,44−46] The relative low island density of Au on ZrO_2(111) at room temperature compared to Au on other oxides[40,47,48] or other metal−oxide systems such as Ag/CeO$_{2-x}$-(111)[49,50] and Pt/CeO$_{2-x}$(111)[51] suggests that the interaction between Au and ZrO_2 is rather weak.

It should be mentioned here that, although both the experimental results and thermodynamic prediction strongly suggest that the growth of Au on ZrO_2(111) follows VW mode, it would be helpful to be further confirmed by STM observations that provide more direct structural/morphological information.

3.3. Interfacial Interaction of Au with ZrO_2(111). The electronic structure of small metal clusters may be different from the bulk because of the quantum size effects and/or specific metal−substrate interfacial interaction. The interfacial interaction between the adsorbed metal clusters and the underlying oxide support can be probed by photoemission spectroscopy. From Figure 2, one can clearly see that in addition to the intensity changes, the Au 4f peaks shift to a higher binding energy (BE) as the Au coverage decreases. There is also a pronounced broadening of Au 4f peaks with decreasing Au coverage. In parts a and b of Figure 4, the Au $4f_{7/2}$ BE and full width of half-maximum (fwhm) that were read out from curve-fitting results and varied within 0.05 eV in the repeated experiments are plotted versus Au coverage at room temperature, respectively. At 0.04 ML, the Au 4f spectrum exhibits a broad feature with the $4f_{7/2}$ peak position centered at 84.41 ± 0.05 eV. As the coverage increases, both the Au $4f_{7/2}$ BE and fwhm gradually shift toward the values of bulk metallic Au, which are 84.00 and 1.13 eV, respectively. At 6.25 ML Au coverage, each approaches the bulk value.

In principle, the BE shifts for small metallic particles deposited onto poorly conducting substrates can be contributed from either the initial-state (intrinsic size effect due to reduced average coordination number and charge exchange between metal and the substrate)[52,53] or final-state (relaxation and screening)[54,55] effects, or both. Auger parameter method[56,57] has been regarded as an effective approach for differentiating the initial- and final-state effects in core-level BE shifts. In the present work, however, it is difficult to use this method to distinguish the initial- and final-state effects in the Au $4f_{7/2}$ BE shifts because the Au Auger peaks are too weak at very low coverages to identify the peak positions. Nevertheless, it is worth emphasizing here that the Au $4f_{7/2}$ BE shifts only by 0.41 ± 0.05 eV from very low (0.04 ML) to high (6.25 ML) Au coverages. This value is smaller than those observed for Au on similar irreducible oxides such as SiO_2[58] and Al_2O_3[59] where only the final-state effects were found to be responsible for the core-level BE shifts. In general, a core hole created during the photoionization of the core electrons in the metal clusters could be effectively screened if the substrate is a conductor, an electron from the substrate hops onto the cluster to neutralize the instantaneous charge produced during the time relevant to the photoemission.[60] That is the case of a complete hole delocalization.[61] However, if the metal clusters deposited onto a relatively less conductive substrate, the core-level shifts are probably larger due to the hole localization in the final state.[62] This means that, if only the final-state effects are taken into account for the core-level BE shifts, the core holes in the metal clusters are better screened on the more conductive substrates, leading to a smaller BE shifts. It was found that different Au $4f_{7/2}$ BE shifts were observed for Au clusters on different oxides: 0.6 eV on TiO_2,[63] 0.3 eV on CeO_2,[64] 1.4 eV on Al_2O_3,[59] 1.6 eV on SiO_2,[58] and 0.65 eV on YSZ.[33] In the present case, the largest Au $4f_{7/2}$ BE shift from small clusters to bulk that we found is substantially smaller than the shifts for Au on other irreducible oxide substrates (e.g., Al_2O_3, SiO_2, YSZ) but is rather analogous to the shifts observed for Au on reducible oxide substrates (e.g., TiO_2, CeO_2). Considering the fact that reducible oxides are usually more conductive than irreducible oxides due to the easy formation of oxygen defects, the reducible oxides should have higher abilities of active substrates to shield the final-state core holes via extra-atomic relaxation than irreducible oxides.[65] Provided there was no initial-state contribution to the Au 4f peak shifts, the final-state screening would lead to the Au $4f_{7/2}$ BE shift
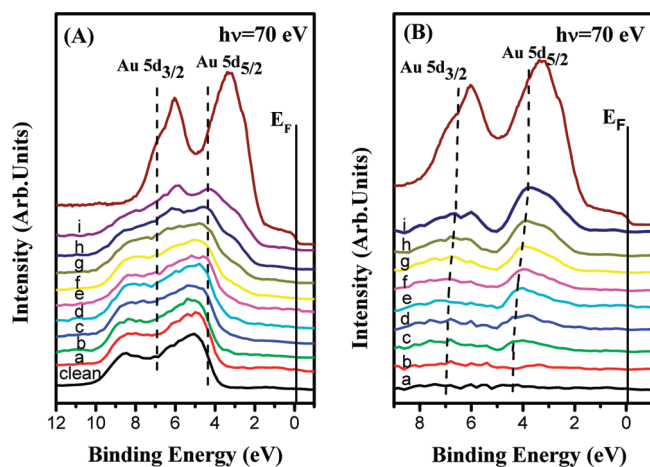
10747

dx.doi.org/10.1021/jp201960t |*J. Phys. Chem. C* 2011, 115, 10744–10751

Figure 5. (A) Valence band spectra of Au on $ZrO_2(111)$ at room temperature for Au coverage of 0.04, 0.21, 0.46, 0.63, 0.83, 1.25, 2.08, 4.17, and 6.25 ML, which are labeled as (a)−(i), respectively. (B) The difference spectra from (A) with the clean ZrO_2 surface subtracted. The top curve shows the valence band spectrum from a clean Au polycrystal sample.

Figure 6. Au 4f peak areas of 0.25 and 1 ML Au, normalized to their initial values respectively on the $ZrO_2(111)$ surface as a function of the annealing temperature.

for Au on $ZrO_2(111)$ being as large as or close to those on other irreducible oxide substrates, other than analogous to those on reducible oxide substrates. To a first approximation, the core-level BE of Au should be raised by $e^2/2R$ with respect to that of bulk Au, where R is the radius of metal particles.[67] As mentioned above, the average radius of Au particles can be estimated at any given Au coverage by assuming a constant island density. At 0.04 ML of Au, the average diameter of Au particles is 14.2 Å, and thus the shift of Au BE should be about 1.02 eV relative to the bulk Au. Therefore, the small BE shift of Au $4f_{7/2}$ observed for Au on $ZrO_2(111)$ provides a strong evidence for the contribution of initial-state effects. As mentioned above, the initial-state contribution may originate from: (1) intrinsic size effects due to reduced metal−metal coordination, and (2) electron charge transfer between metal and substrate. When the particle size is very small, the surface atoms dominate, leading to the lower coordination number compared to bulk atoms. Thus, the initial-state contribution to the Au 4f BE shifts originated from the reduced metal−metal coordination number would be equivalent to the surface core-level shifts (SCLS) of Au metal, which was reported to be −0.4 eV.[66] This is the main contribution to the initial-state effects. Besides this, there should be another factor that can compensate more than −0.2 eV because the total Au 4f BE shift is only 0.4 eV. We attribute this to the formation of negatively charged Au at very low coverages. Similar gold species have also been observed previously for Au growth on YSZ-(100)[26] and thin MgO/Fe(001) films,[67] where Au carries initially a negative charge relative to the bulk. However, during the deposition of Au on $ZrO_2(111)$, the binding energies of Zr 3d (part b of Figure 2) and O 1s (not shown) show no shifts until 2.17 ML Au. Afterward, they both shift to low BE by 0.22 ± 0.05 eV when the coverage reaches 6.25 ML, which can be explained by the effective screening from the large gold clusters on the zirconia film.[57,68] Because both Zr 3d and O 1s show no BE shifts at low coverages, the chief cause of negatively charged Au may be the result of Au initially bonding to the surface defect sites such as oxygen vacancies or steps/kinks, leading to the partial charge transfer from zirconia to gold.
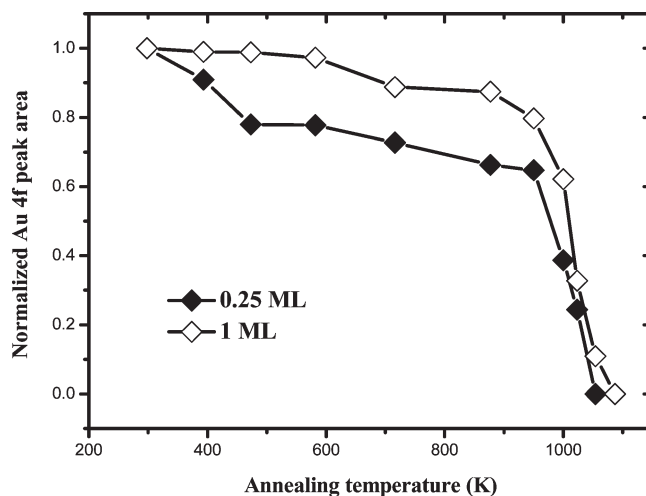
The line width of the Au $4f_{7/2}$ peak increases with decreasing particle size (part b of Figure 4). The increased line width can mainly result from the particle size and particle size distribution.[69,70] That is, when the particles are very small in size and have a broad size distribution, the line width gets broader. As the Au coverage increases, the Au particles grow larger in size and become more homogeneous as compared to those at low coverages. Accordingly, the line width of the Au $4f_{7/2}$ peak is narrowed.

Part A of Figure 5 shows the valence band spectra of Au/$ZrO_2(111)$ at various Au coverages at 300 K with an excitation energy of 70 eV. For comparison, the spectrum from a clean Au foil is shown as the top curve. As can be seen, the valence band of the clean $ZrO_2(111)$ surface is dominated by the O 2p and Zr 4d orbitals locating at 3−10 eV below E_F, in good agreement with previously reported results.[30,71] After Au is deposited, because of the contribution of the Au 5d band, the valence band between 3 and 10 eV changes in shape and becomes broader. Because of the fact of serious BE overlapping between Au 5d and O 2p and Zr 4d bands, it is difficult to identify the Au 5d itself alone just from the spectra. To differentiate the Au 5d band, we took the difference spectra with respect to the clean $ZrO_2(111)$ surface. The results are plotted in part B of Figure 5. It is known that Au exhibits a well-defined d-band doublet ($5d_{5/2}$ and $5d_{3/2}$) in the valence band. With increasing Au coverage, this doublet splitting can be clearly seen. Moreover, similar to the observation of Au 4f, both peaks of Au $5d_{5/2}$ and $5d_{3/2}$ gradually shift toward the Fermi edge (i.e., lower BE), but the shift of Au $5d_{5/2}$ is more evident and larger than the shift of Au $5d_{3/2}$. In other words, the splitting of Au 5d becomes larger and larger as the Au coverage increases. Nevertheless, there is a still significant difference in the Au 5d spectra between the Au particles and pure Au metal. This difference can be interpreted as the redistribution of the Au 5d valence band with decreasing particle size. A similar phenomenon has also been found for Au on other oxide surfaces.[33,72−76] Because the Au $5d_{5/2}$ and $5d_{3/2}$ splitting is strongly dependent on the average coordination number of Au nearest neighbors or Au cluster size (the splitting value varies from 1.5 eV for single Au atoms to 2.7 eV for bulk Au),[33,61,65] the coverage-dependent Au 5d splitting observed here can be used to estimate the average
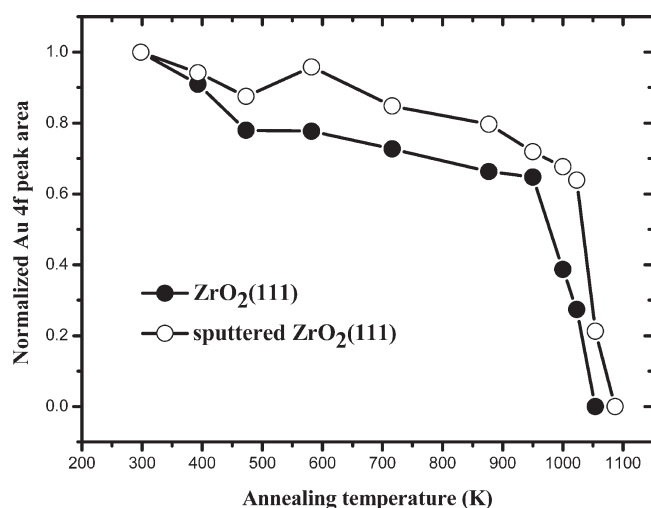
Figure 7. Au 4f peak areas of 0.25 ML Au, normalized to the initial values, on the $ZrO_2(111)$ and sputtered $ZrO_2(111)$ surfaces as a function of annealing temperature. The details for the sputtered ZrO_2-(111) surface preparation can be found in the text.

coordination number of Au atoms in the particles. As the Au coverage increases to 0.46 ML, the Au 5d splitting in part B of Figure 5 starts to become distinguishable and exhibits a value of ∼2.5 eV; it reaches to ∼2.7 eV when the coverage increases up to 6.25 ML. According to the literature,[65,33] the Au 5d splitting of 2.5 and 2.7 eV corresponds roughly to the mean coordination number of Au atoms of 10 and 12, respectively. The coordination number of 10 at 0.46 ML suggests that, at this coverage the average Au particle size is already large, consistent with the above-mentioned observation of small island density. However, the reduced coordination number at low coverages as confirmed by the observation of Au 5d again supports the above discussion of initial-state effects in the Au 4f BE shifts.

3.4. Thermal Stability of Au/ZrO₂(111). To investigate the thermal stability of Au nanoparticles on $ZrO_2(111)$, we annealed the $ZrO_2(111)$ surface covered with Au particles at 300 K to elevated temperatures, after which photoemission spectra were collected at 300 K. The data of annealing experiments on ZrO_2-(111) covered with 0.25 and 1 ML Au are illustrated in Figure 6, respectively. The Au 4f peak areas were normalized to their own initial values with the purpose of clearly displaying the variation trend of Au 4f peak intensities as a function of the annealing temperature. Upon heating, the Au 4f intensities decrease for both surfaces but more rapidly on 0.25 ML Au-covered ZrO_2-(111). The sharp decrease in Au 4f intensities occurs at temperatures above 950 and 1000 K for the surfaces covered with 0.25 and 1 ML Au, respectively. By annealing to 1090 K, no Au signal is detected for both Au/$ZrO_2(111)$ surfaces.

The interpretation of the decrease of Au 4f peak intensities at elevated temperatures can be related to many factors, such as an encapsulation of Au clusters by ZrO_2, diffusion of Au into the substrate, aggregation of Au small particles into large particles (i.e., sintering), and desorption of Au from the surface. Here, within the temperature region between 300 to 950 K for 0.25 ML Au and 300 to 1000 K for 1 ML Au, the gradual decrease in Au 4f intensities can be attributed to the sintering of Au particles instead of encapsulation and diffusion because there is no change in the position and the line width of Zr 3d XPS peaks (spectra not shown). In addition, Ar^+-sputtering depth profile experiments

also rule out the possibilities of encapsulation and diffusion. Moreover, with increasing annealing temperature both Au 4f BE and fwhm (spectra not shown) decrease, suggesting that Au particles sinter into large ones. Further annealing to above 1000 K causes a sharp decrease of Au 4f peak intensity. This correlates with Au desorption from the $ZrO_2(111)$ surface. The desorption of Au from oxide surfaces above 1000 K has been also found for Au/SiO_2[58] and Au/TiO_x.[77−79] From Figure 6, one can clearly see that at higher coverage the Au particles are more thermally stable. Alternatively speaking, the larger Au particles are more thermally stable than the smaller ones on $ZrO_2(111)$, which might be explained by the fact that the small Au particles undergo sintering not only by the Ostwald ripening but also by facile diffusion on the surface and coalesce, whereas the large particles might sinter mainly through the Ostwald ripening.[80] Moreover, the small particles desorb more easily than the large ones because of the lower coordination number of Au atoms and decreased surface tension in the small particles.[58]

To examine the effects of surface defects on the thermal stability of Au nanoparticles on $ZrO_2(111)$, we deposited 0.25 ML Au on the sputtered $ZrO_2(111)$ surface at 300 K and then monitored the Au 4f intensities at different annealing temperatures. The results are shown in Figure 7. For comparison, the results of similar experiments with the same coverage of Au on the pristine $ZrO_2(111)$ surface are also shown here. The sputtered ZrO_2-(111) surface was obtained by dosing 1.1 MLE Ar^+ ions with a kinetic energy of 1000 eV on $ZrO_2(111)$ at 300 K, where 1 MLE represents a dosage of 1.4×10^{15} ions/cm². As can be seen, the Au particles are obviously more thermally stable on sputtered $ZrO_2(111)$ than on pristine $ZrO_2(111)$. Apparently, the sputtered $ZrO_2(111)$ surface exhibits sinter resistance of supported Au particles. It is well-known that surface sputtering creates many kinds of surface defects such as oxygen vacancies, kinks, and holes. The higher thermal stability of Au particles on the sputtered $ZrO_2(111)$ surface can thus be attributed to the stronger bonding of Au to the defect sites. This agrees very well with previous results where surface defects were found to play an important role in the nucleation, growth, and stability of metal clusters on oxide surfaces.[81]

4. CONCLUSIONS

In this work, we studied the growth, electronic properties, and thermal stability of Au nanoparticles on the $ZrO_2(111)$ thin films, which were grown on the Pt(111) substrate, using LEED, SRPES, and XPS. At room temperature, Au most likely grows two dimensionally on $ZrO_2(111)$ up to 0.1 ML followed by 3D growth. The Au $4f_{7/2}$ BE shifts toward a higher BE with decreasing the Au particle size by 0.4 eV, which can be attributed to the contribution from both the initial- and final-state effects. The initial-state effects, which mainly exist at very low coverages, include the reduced coordination number of Au atoms and probably the charge transfer from $ZrO_2(111)$ to Au particles. At high coverages where the particle size increases, the final-state effects dominate. No strong interfacial interaction between Au particles and $ZrO_2(111)$ can be observed. Annealing of Au/$ZrO_2(111)$ under UHV conditions leads to significant aggregation of Au small clusters into large particles before they desorb from the surface. Surface defects are proven to be able to enhance the thermal stability of Au particles on $ZrO_2(111)$ due to the stronger bonding of Au atoms on these sites.

10749

dx.doi.org/10.1021/jp201960t |*J. Phys. Chem. C* 2011, 115, 10744–10751

■ AUTHOR INFORMATION

Corresponding Author
*E-mail: jfzhu@ustc.edu.cn.

■ ACKNOWLEDGMENT

■ REFERENCES

(1) Haruta, M.; Yamada, N.; Kobayashi, T.; Iijima, S. Gold catalysts prepared by coprecipitation for low-temperature oxidation of hydrogen and of carbon-monoxide. *J. Catal.* **1989**, *115*, 301–309.

(2) Haruta, M.; Date, M. Advances in the catalysis of Au nanoparticles. *Appl. Catal. A: Gen.* **2001**, *222*, 427–437.

(3) Meyer, R.; Lemire, C.; Shaikhutdinov, S. K.; Freund, H. Surface chemistry of catalysis by gold. *Gold Bull.* **2004**, *37*, 72–124.

(4) Lin, S. D.; Bollinger, M.; Vannice, M. A.; Low-temperature CO oxidation over Au/TiO₂ and Au/SiO₂ catalysts. *Catal. Lett.* **1993**, *17*, 245–262.

(5) Overbury, S. H.; Ortiz-Soto, L.; Zhu, H. G.; Lee, B.; Amiridis, M. D.; Dai, S. Comparison of Au catalysts supported on mesoporous titania and silica: Investigation of Au particle size effects and metal-support interactions. *Catal. Lett.* **2004**, *95*, 99–106.

(6) Schubert, M. M.; Hackenberg, S.; van Veen, A. C.; Muhler, M.; Plzak, V.; Behm, R. J. CO oxidation over supported gold catalysts - "inert" and "active" support materials and their role for the oxygen supply during reaction. *J. Catal.* **2001**, *197*, 113–122.

(7) Liotta, L. F.; Di Carlo, G.; Pantaleo, G.; Venezia, A. M. Supported gold catalysts for CO oxidation and preferential oxidation of CO in H₂ stream: Support effect. *Catal. Today* **2010**, *158*, 56–62.

(8) Ivanova, S.; Pitchon, V.; Petit, C.; Caps, V. Support effects in the gold-catalyzed preferential oxidation of CO. *Chemcatchem* **2010**, *2*, 556–563.

(9) Fu, Q.; Saltsburg, H.; Flytzani-Stephanopoulos, M. Active non-metallic Au and Pt species on ceria-based water-gas shift catalysts. *Science* **2003**, *301*, 935–938.

(10) Manzoli, M.; Boccuzzi, F.; Chiorino, A.; Vindigni, F.; Deng, W. L.; Flytzani-Stephanopoulos, M. Spectroscopic features and reactivity of CO adsorbed on different Au/CeO₂ catalysts. *J. Catal.* **2007**, *245*, 308–315.

(11) Rodriguez, J. A.; Wang, X.; Liu, P.; Wen, W.; Hanson, J. C.; Hrbek, J.; Perez, M.; Evans, J. Gold nanoparticles on ceria: Importance of O vacancies in the activation of gold. *Top. Catal.* **2007**, *44*, 73–81.

(12) Tibiletti, D.; Amieiro-Fonseca, A.; Burch, R.; Chen, Y.; Fisher, J. M.; Goguet, A.; Hardacre, C.; Hu, P.; Thompsett, A. DFT and in situ EXAFS investigation of gold/ceria-zirconia low-temperature water gas shift catalysts: Identification of the nature of the active form of gold. *J. Phys. Chem. B* **2005**, *109*, 22553–22559.

(13) Idakiev, V.; Tabakova, T.; Naydenov, A.; Yuan, Z. Y.; Su, B. L. Gold catalysts supported on mesoporous zirconia for low-temperature water-gas shift reaction. *Appl. Catal. B: Environ.* **2006**, *63*, 178–186.

(14) Li, J.; Chen, J. L.; Song, W.; Liu, J. L.; Shen, W. J. Influence of zirconia crystal phase on the catalytic performance of Au/ZrO₂ catalysts for low-temperature water gas shift reaction. *Appl. Catal. A: Gen.* **2008**, *334*, 321–329.

(15) Zhang, X.; Shi, H.; Xu, B. Q. Comparative study of Au/ZrO₂ catalysts in CO oxidation and 1,3-butadiene hydrogenation. *Catal. Today* **2007**, *122*, 330–337.

(16) Rossignol, S.; Madier, Y.; Duprez, D. Preparation of zirconia-ceria materials by soft chemistry. *Catal. Today* **1999**, *50*, 261–270.

(17) Fally, F.; Perrichon, V.; Vidal, H.; Kaspar, J.; Blanco, G.; Pintado, J. M.; Bernal, S.; Colon, G.; Daturi, M.; Lavalley, J. C. Modification of the oxygen storage capacity of CeO₂-ZrO₂ mixed oxides after redox cycling aging. *Catal. Today* **2000**, *59*, 373–386.

(18) Comotti, M.; Li, W. C.; Spliethoff, B.; Schuth, F. Support effect in high activity gold catalysts for CO oxidation. *J. Am. Chem. Soc.* **2006**, *128*, 917–924.

(19) Azizi, Y.; Pitchon, V.; Petit, C. Effect of support parameters on activity of gold catalysts: Studies of ZrO₂, TiO₂ and mixture. *Appl. Catal. A: Gen.* **2010**, *385*, 170–177.

(20) Manzoli, M.; Boccuzzi, F.; Trevisan, V.; Menegazzo, F.; Signoretto, M.; Pinna, F. Au/ZrO₂ catalysts for LT-WGSR: Active role of sulfates during gold deposition. *Appl. Catal. B: Environ.* **2010**, *96*, 28–33.

(21) Zhang, X.; Shi, H.; Xu, B. Q. Catalysis by gold: Isolated surface Au³⁺ ions are active sites for selective hydrogenation of 1,3-butadiene over Au/ZrO₂ catalysts. *Angew. Chem. Int. Ed.* **2005**, *44*, 7132–7135.

(22) McEwan, L.; Julius, M.; Roberts, S.; Fletcher, J. C. Q. A review of the use of gold catalysts in selective hydrogenation reactions. *Gold Bull.* **2010**, *43*, 298–306.

(23) Li, J.; Ta, N.; Song, W.; Zhan, E. S.; Shen, W. J. Au/ZrO₂ catalysts for low-temperature water gas shift reaction: Influence of particle sizes. *Gold Bull.* **2009**, *42*, 48–60.

(24) Zhang, X.; Wang, H.; Xu, B. Q. Remarkable nanosize effect of zirconia in Au/ZrO₂ catalyst for CO oxidation. *J. Phys. Chem. B* **2005**, *109*, 9678–9683.

(25) Zane, F.; Trevisan, V.; Pinna, F.; Signoretto, M.; Menegazzo, F. Investigation on gold dispersion of Au/ZrO₂ catalysts and activity in the low-temperature WGS reaction. *Appl. Catal. B: Environ.* **2009**, *89*, 303–308.

(26) Zafeiratos, S.; Neophytides, S.; Kennou, S. A photoelectron spectroscopy study of Au thin films on ZrO₂(100). *Thin Solid Films* **2001**, *386*, 53–58.

(27) Munoz, M. C.; Gallego, S.; Beltran, J. I.; Cerda, J. Adhesion at metal-ZrO₂ interfaces. *Surf. Sci. Rep.* **2006**, *61*, 303–344.

(28) Grau-Crespo, R.; Hernandez, N. C.; Sanz, J. F.; de Leeuw, N. H. Theoretical investigation of the deposition of Cu, Ag, and Au atoms on the ZrO₂(111) surface. *J. Phys. Chem. C* **2007**, *111*, 10448–10454.

(29) Wang, C. M.; Fan, K. N.; Liu, Z. P. Origin of oxide sensitivity in gold-based catalysts: A first principle study of CO oxidation over Au supported on monoclinic and tetragonal ZrO₂. *J. Am. Chem. Soc.* **2007**, *129*, 2642–2647.

(30) Gao, Y.; Zhang, L.; Pan, Y. H.; Wang, G. D.; Xu, Y.; Zhang, W. H.; Zhu, J. F. Epitaxial growth of ultrathin ZrO₂(111) films on Pt(111). *Chin. Sci. Bull.* **2011**, *56*, 502–507.

(31) Meinel, K.; Eichler, A.; Schindler, K. M.; Neddermeyer, H. STM, LEED, and DFT characterization of epitaxial ZrO₂ films on Pt(111). *Surf. Sci.* **2004**, *562*, 204–218.

(32) Meinel, K.; Hofmann, A.; Forster, S.; Kulla, R.; Schindler, K. M.; Neddermeyer, H.; Sauer, J.; Widdra, W. Interaction of SO₃ with c-ZrO₂-(111) films on Pt(111). *Phys. Chem. Chem. Phys.* **2006**, *8*, 1593–1600.

(33) Zafeiratos, S.; Kennou, S. A study of gold ultrathin film growth on yttria-stabilized ZrO₂(100). *Surf. Sci.* **1999**, *443*, 238–244.

(34) Zhu, J. F.; Kinne, M.; Fuhrmann, T.; Denecke, R.; Steinruck, H. P. In situ high-resolution XPS studies on adsorption of NO on Pt(111). *Surf. Sci.* **2003**, *529*, 384–396.

(35) Meinel, K.; Eichler, A.; Forster, S.; Schindler, K. M.; Neddermeyer, H.; Widdra, W. Surface and interface structures of epitaxial ZrO₂ films on Pt(111): Experiment and density-functional theory calculations. *Phys. Rev. B* **2006**, *74*, 235444(1–11).

(36) Memeo, R.; Ciccacci, F.; Mariani, C.; Ossicini, S. On the use of the auger technique for quantitative-analysis of overlayers. *Thin Solid Films* **1983**, *109*, 159–167.

(37) Zhu, J. F.; Farmer, J. A.; Ruzycki, N.; Xu, L.; Campbell, C. T.; Henkelman, G. Calcium adsorption on MgO(100): Energetics, structure, and role of defects. *J. Am. Chem. Soc.* **2008**, *130*, 2314–2322.

(38) Tanuma, S.; Powell, C. J.; Penn, D. R. Calculations of electron inelastic mean free paths for 31 materials. *Surf. Interface Anal.* **1988**, *11*, 577–589.

(39) Zhang, L.; Persaud, R.; Madey, T. E. Ultrathin metal films on a metal oxide surface: Growth of Au on TiO₂(110). *Phys. Rev. B* **1997**, *56*, 10549–10557.

(40) Lai, X.; St Clair, T. P.; Valden, M.; Goodman, D. W. Scanning tunneling microscopy studies of metal clusters supported on TiO₂(110): Morphology and electronic structure. *Prog. Surf. Sci.* **1998**, *59*, 25–52.

(41) Campbell, C. T. Ultrathin metal films and particles on oxide surfaces: Structural, electronic and chemisorptive properties. *Surf. Sci. Rep* **1997**, *27*, 1–111.

(42) Chatain, D.; Rivollet, I.; Eustathopoulos, N. Thermodynamic adhesion in nonreactive liquid metal-alumina systems. *J. Chim. Phys. Phys. - Chim. Biol.* **1986**, *83*, 561–567.

(43) Chatain, D.; Rivollet, I.; Eustathopoulos, N. Estimation of the thermodynamic adhesion and the contact-angle in the nonreactive metal-ionocovalent oxide systems. *J. Chim. Phys. Phys. - Chim. Biol.* **1987**, *84*, 201–203.

(44) Yakshinskiy, B.; Akbulut, M.; Madey, T. E. Transmission of low-energy (<10 eV) O⁺ ions through Au films on TiO₂(110). *Surf. Sci.* **1997**, *390*, 132–139.

(45) Ernst, K. H.; Ludviksson, A.; Zhang, R.; Yoshihara, J.; Campbell, C. T. Growth-model for metal-films on oxide surfaces - Cu on ZnO-(0001)-O. *Phys. Rev. B* **1993**, *47*, 13782–13796.

(46) Parker, S. C.; Grant, A. W.; Bondzie, V. A.; Campbell, C. T. Island growth kinetics during the vapor deposition of gold onto TiO₂-(110). *Surf. Sci.* **1999**, *441*, 10–20.

(47) Lu, J. L.; Gao, H. J.; Shaikhutdinov, S.; Freund, H. J. Gold supported on well-ordered ceria films: Nucleation, growth and morphology in CO oxidation reaction. *Catal. Lett.* **2007**, *114*, 8–16.

(48) Zhou, Y. H.; Zhou, J. Growth and sintering of Au-Pt nanoparticles on oxidized and reduced CeO$_x$(111) thin films by scanning tunneling microscopy. *J. Phys. Chem. Lett.* **2010**, *1*, 609–615.

(49) Farmer, J. A.; Baricuatro, J. H.; Campbell, C. T. Ag adsorption on reduced CeO₂(111) thin films. *J. Phys. Chem. C* **2010**, *114*, 17166–17172.

(50) Kong, D. D.; Wang, G. D.; Pan, Y. H.; Hu, S. W.; Hou, J. B.; Pan, H. B.; Campbell, C. T.; Zhu, J. F. Growth, structure and stability of Ag on CeO₂(111): Synchrotron radiation photoemission studies. *J. Phys. Chem. C* **2011**, *115*, 6715–6725.

(51) Zhou, Y. H.; Perket, J. M.; Zhou, J. Growth of Pt nanoparticles on reducible CeO₂(111) thin films: Effect of nanostructures and redox properties of ceria. *J. Phys. Chem. C* **2010**, *114*, 11853–11860.

(52) Steinruck, H. P.; Pesty, F.; Zhang, L.; Madey, T. E. Ultrathin films of Pt on TiO₂(110) - Growth and chemisorption-induced surfactant effects. *Phys. Rev. B* **1995**, *51*, 2427–2439.

(53) Bagus, P. S.; Brundle, C. R.; Pacchioni, G.; Parmigiani, F. Mechanisms responsible for the shifts of core-level binding-energies between surface and bulk atoms of metals. *Surf. Sci. Rep.* **1993**, *19*, 265–283.

(54) Rodriguez, J. A.; Kuhn, M.; Hrbek, J. Interaction of silver, cesium, and zinc with alumina surfaces: Thermal desorption and photoemission studies. *J. Phys. Chem.* **1996**, *100*, 18240–18248.

(55) Wertheim, G. K.; Dicenzo, S. B.; Buchanan, D. N. E. Noble- and transition-metal clusters: The d bands of silver and palladium. *Phys. Rev. B* **1986**, *33*, 5384–5390.

(56) Wagner, C. D. Auger lines in x-ray photoelectron spectrometry. *Anal. Chem.* **1972**, *44*, 967–973.

(57) Luo, K.; Lai, X.; Yi, C. W.; Davis, K. A.; Gath, K. K.; Goodman, D. W. The growth of silver on an ordered alumina surface. *J. Phys. Chem. B* **2005**, *109*, 4064–4068.

(58) Chusuei, C. C.; Lai, X.; Luo, K.; Goodman, D. W. Modeling heterogeneous catalysts: Metal clusters on planar oxide supports. *Top. Catal.* **2001**, *14*, 71–83.

(59) Luo, M. F.; Shiu, H. W.; Ten, M. H.; Sartale, S. D.; Chiang, C. I.; Lin, Y. C.; Hsu, Y. J. Growth and electronic properties of Au nanoclusters on thin-film Al₂O₃/NiAl(100) studied by scanning tunnelling microscopy and photoelectron spectroscopy with synchrotron radiation. *Surf. Sci.* **2008**, *602*, 241–248.

(60) Wertheim, G. K.; Dicenzo, S. B.; Youngquist, S. E. Unit charge on supported gold clusters in photoemission final-state. *Phys. Rev. Lett.* **1983**, *51*, 2310–2313.

(61) Egelhoff, W. F., Jr. Core-level binding-energy shifts at surfaces and in solids. *Surf. Sci. Rep.* **1986**, *6*, 253–415.

(62) Parmigiani, F.; Kay, E.; Bagus, P. S.; Nelin, C. J. Core binding-energies for clusters deposited on different insulating substrates - ESCA spectra and theoretical electronic-structure studies. *J. Electron Spectrosc. Relat. Phenom.* **1985**, *36*, 257–267.

(63) Jiang, Z. Q.; Zhang, W. H.; Jin, L.; Yang, X.; Xu, F. Q.; Zhu, J. F.; Huang, W. X. Direct XPS evidence for charge transfer from a reduced rutile TiO₂(110) surface to Au clusters. *J. Phys. Chem. C* **2007**, *111*, 12434–12439.

(64) Weststrate, C. J.; Resta, A.; Westerstrom, R.; Lundgren, E.; Mikkelsen, A.; Andersen, J. N. CO adsorption on a Au/CeO₂(111) model catalyst. *J. Phys. Chem. C* **2008**, *112*, 6900–6906.

(65) Mason, M. G. Electronic-structure of supported small metal-clusters. *Phys. Rev. B* **1983**, *27*, 748–762.

(66) Johansson, B.; Martensson, N. Core-level binding-energy shifts for the metallic elements. *Phys. Rev. B* **1980**, *21*, 4427–4457.

(67) Torelli, P.; Giordano, L.; Benedetti, S.; Luches, P.; Annese, E.; Valeri, S.; Pacchioni, G. X-ray photoemission study of the charge state of Au nanoparticles on thin MgO/Fe(001) films. *J. Phys. Chem. C* **2009**, *113*, 19957–19965.

(68) Luo, K.; Kim, D. Y.; Goodman, D. W. The nucleation and growth of gold on silica. *J. Mol. Catal. A: Chem* **2001**, *167*, 191–198.

(69) Cheung, T. T. P. X-ray photoemission of small platinum and palladium clusters. *Surf. Sci.* **1984**, *140*, 151–164.

(70) Luo, K.; St Clair, T. P.; Lai, X.; Goodman, D. W. Silver growth on TiO₂(110)(1 × 1) and (1 × 2). *J. Phys. Chem. B* **2000**, *104*, 3050–3057.

(71) Sanz, J. M.; Gonzalezelipe, A. R.; Fernandez, A.; Leinen, D.; Galan, L.; Stampfl, A.; Bradshaw, A. M. A resonant photoemission-study of the ZrO₂ valence-band. *Surf. Sci.* **1994**, *307*, 848–853.

(72) Peto, G.; Molnar, G. L.; Paszti, Z.; Geszti, O.; Beck, A.; Guczi, L. Electronic structure of gold nanoparticles deposited on SiO$_x$/Si(100). *Mater. Sci. Eng., C* **2002**, *19*, 95–99.

(73) Guczi, L.; Peto, G.; Beck, A.; Frey, K.; Geszti, O.; Molnar, G.; Daroczi, C. Gold nanoparticles deposited on SiO₂/Si(100): Correlation between size, electron structure, and activity in CO oxidation. *J. Am. Chem. Soc.* **2003**, *125*, 4332–4337.

(74) Paszti, Z.; Peto, G.; Horvath, Z. E.; Karacs, A.; Guczi, L. Formation and valence band density of states of nonspherical Cu nanoparticles deposited on Si(100) substrate. *J. Phys. Chem. B* **1997**, *101*, 2109–2115.

(75) Chen, M. S.; Cai, Y.; Yan, Z.; Goodman, D. W. On the origin of the unique properties of supported Au nanoparticles. *J. Am. Chem. Soc.* **2006**, *128*, 6341–6346.

(76) Howard, A.; Clark, D. N. S.; Mitchell, C. E. J.; Egdell, R. G.; Dhanak, V. R. Initial and final state effects in photoemission from Au nanoclusters on TiO₂(110). *Surf. Sci.* **2002**, *518*, 210–224.

(77) Chen, M. S.; Goodman, D. W. Catalytically active gold on ordered titania supports. *Chem. Soc. Rev.* **2008**, *37*, 1860–1870.

(78) Xu, C.; Oh, W. S.; Liu, G.; Kim, D. Y.; Goodman, D. W. Characterization of metal clusters (Pd and Au) supported on various metal oxide surfaces (MgO and TiO₂). *J. Vac. Sci. Technol., A* **1997**, *15*, 1261–1268.

(79) Chen, M. S.; Luo, K.; Kumar, D.; Wallace, W. T.; Yi, C. W.; Gath, K. K.; Goodman, D. W. The structure of ordered Au films on TiO$_x$. *Surf. Sci.* **2007**, *601*, 632–637.

(80) Yu, X.; Xu, L. S.; Zhang, W. H.; Jiang, Z. Q.; Zhu, J. F.; Huang, W. X. Synchrotron-radiation photoemission study of growth and stability of Au clusters on rutile TiO₂(110)-1 × 1. *Chin. J. Chem. Phys.* **2009**, *22*, 339–345.

(81) Wallace, W. T.; Min, B. K.; Goodman, D. W. The stabilization of supported gold clusters by surface defects. *J. Mol. Catal. A: Chem* **2005**, *228*, 3–10.